$X_2(YY^*)Z$ X = 3d, Y =4d, Y* = 4f

X = 8A: Pd
Y = 3A: Y
Y* = 4A: Dy
Z = 4B: Sn

$Pd_2Y_{1-x}Dy_xSn$

Heusler alloys with the $L2_1$ structure form at all compositions $0 \leq x \leq 1$. Depending upon composition the compounds are superconducting or antiferromagnetic.

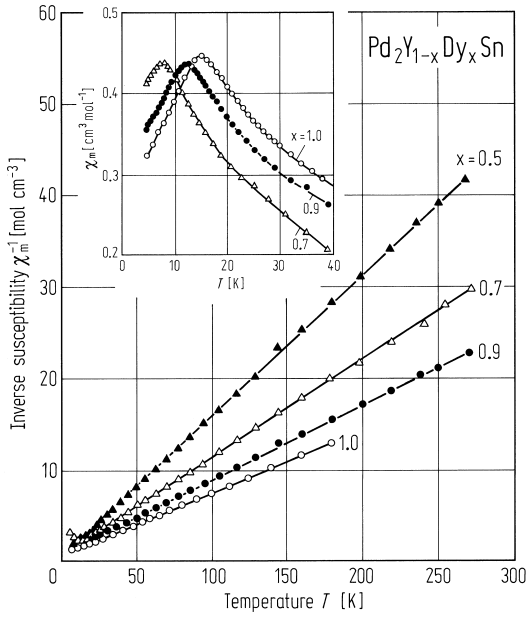

Fig. 198. Susceptibility and reciprocal susceptibility vs. temperature for several $Pd_2(Y_{1-x}Dy_x)Sn$ alloys [86M2].

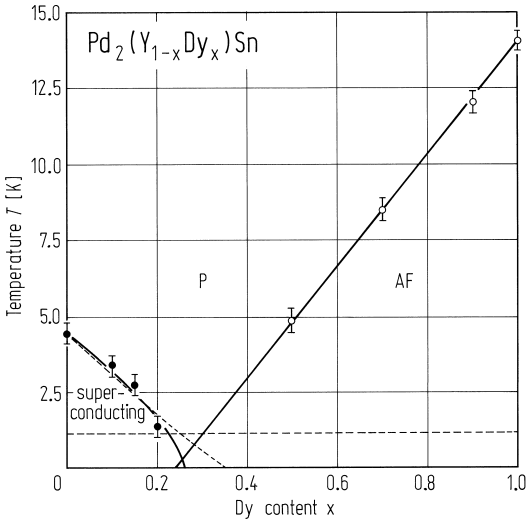

Fig. 199. Magnetic phase diagram of $Pd_2(Y_{1-x}Dy_x)Sn$. The dashed line represents the lowest temperature at which χ_{ac} measurements were made [86M2].

1.5.5.4 Neutron scattering

Details of the neutron scattering technique and the information which can be obtained were discussed in the earlier review [88W1].

1.5.5.4.1 Neutron diffraction

Neutron diffraction enables both the crystallographic and magnetic structures to be determined. To date the majority of investigations have been carried out on powders, using a profile refinement technique. The weak interaction of neutrons with matter, and the fact that the scattering amplitudes do not vary sequentially from element to element means that they are more attractive than X-rays for structural investigations. This is particularly the case if the temperature or pressure is to be changed. Whilst there are an infinite number of ways in which the atoms X_2YZ may arrange themselves in the $L2_1$ structure (see subsect. 1.5.5.2.1) it is normally possible to identify one of the preferential states of atomic order. The most prevalent type of atomic disorder occurring in Heusler alloys is the B2-

type. This type of disorder occurs by the Y and Z atoms exchanging sites. The effect on the diffraction pattern is to reduce the intensity of the odd superlattice reflections with them reduced to zero when the B2 disorder is complete. The two other types of reflection which occur are unaffected by the B2 disorder.

The atomic disorder can also significantly affect the magnetic order. This has been extensively investigated, particularly in the Pd_2MnIn system [88W1]. Measurements on quaternary systems in which In is systematically replaced by Sn or Sb has demonstrated the importance of the electron concentration in establishing the magnetic order. The effect of both atomic order and electron concentration on the magnetic phase diagram are shown in Fig. 200 [92J1] for a system in which the moment is confined to one atom, e.g., Mn. In the case of the $L2_1$ structure, in which the Mn atoms occupy an fcc lattice, there are three main types of commensurate antiferromagnetic structure which occur: types 1, 2 and 3A, which have propagation vectors (001), (111) and ($\frac{1}{2}$10) ($\frac{\bar{1}}{2}$,1,0) which have tetragonal, rhombohedral and orthorhombic symmetry, respectively.

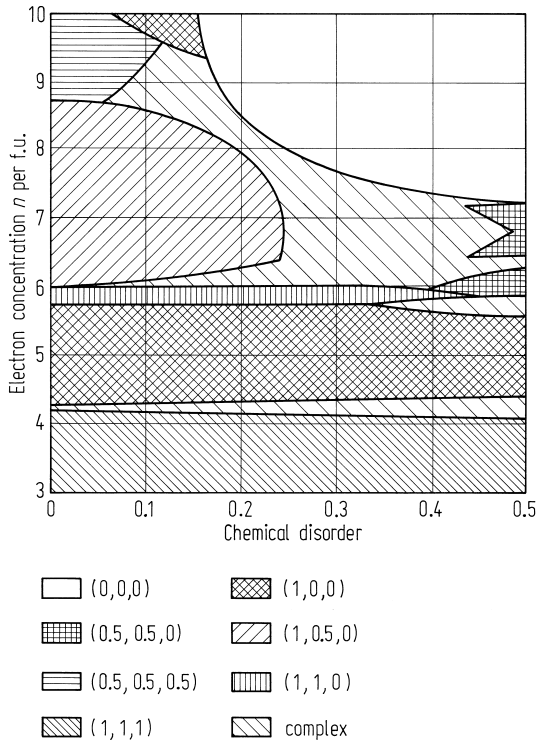

Fig. 200. Magnetic phase diagram as a function of electron concentration and B2 atomic disorder. The propagation vectors for the different magnetic structures are given by the key below. Some magnetic structures refer to a simple cubic lattice. All the other magnetic structures are associated with an fcc lattice. It may be noted that ferromagnetism occurs for complete $L2_1$ order at low electron concentrations [92J1].

X_2YZ X = 3d, Y = 3d

X = 7A: Mn; 8A: Fe, Ni
Y = 5A: V; 7A: Mn; 8A: Ni
Z = 4B: Si, Ge, Sn

$Fe_{3-x}V_xGe$

The atomic order and its effect on the magnetic properties have been investigated using pulsed neutron scattering [90B1]. For $x \leq 0.14$, the hcp DO_{19} structure associated with the parent Fe_3Ge is stable, but beyond this composition the $L2_1$ structure is formed. The neutron measurements suggest that for $0.6 \leq x \leq 1$ the V atoms preferentially occupy one of the Fe sites with magnetisation decreasing with increasing x.

Table 41. Comparison of experimental and theoretical values of the ratios α and β for the alloys in the range $0.6 \le x \le 1.0$. α and β are the normalised nuclear structure factors, namely $\alpha = F^2(111)/F^2(220)$ and $\beta = F^2(200)/F^2(220)$ [90B1].

	Model (i) ($D0_3$)		Model (ii) ($L2_1C$)		Model (iii) ($L2_1A$)		Experimental	
Composition	α [10^{-2}]	β [10^{-2}]	α [10^{-2}]	β [10^{-2}]	α [10^{-2}]	β [10^{-2}]	α [10^{-2}]	β [10^{-2}]
$Fe_{2.4}V_{0.6}Ge$	0.004	0.004	0.19	2.3	2.22	5.61	2.45	5.5
$Fe_{2.2}V_{0.8}Ge$	0.20	0.20	0.22	5.20	5.20	10.36	5.43	9.79
$Fe_{2.0}V_{1.0}Ge$	0.53	0.53	0.25	10.1	10.1	17.61	9.1	18.40

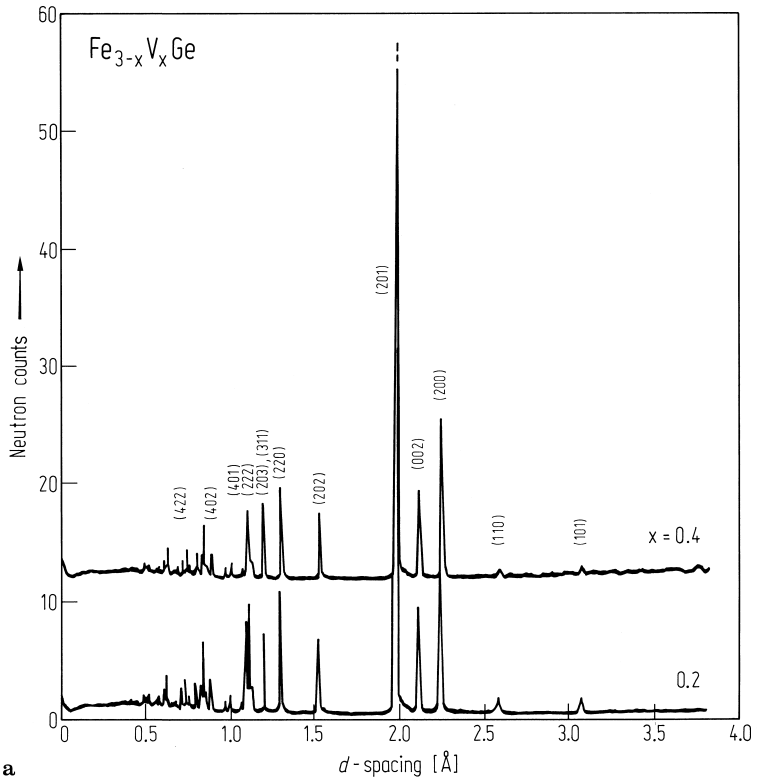

a

Fig. 201. Room temperature neutron diffraction patterns for the $Fe_{3-x}V_xGe$ alloys. (**a**) results for alloys with x = 0.2 and 0.4 indicating a $D0_{19}$-type structure; (**b**) results for $0.6 \le x \le 1.0$ indicating an $L2_1$ structure. The asterisks indicate an additional unidentified phase [90B1].

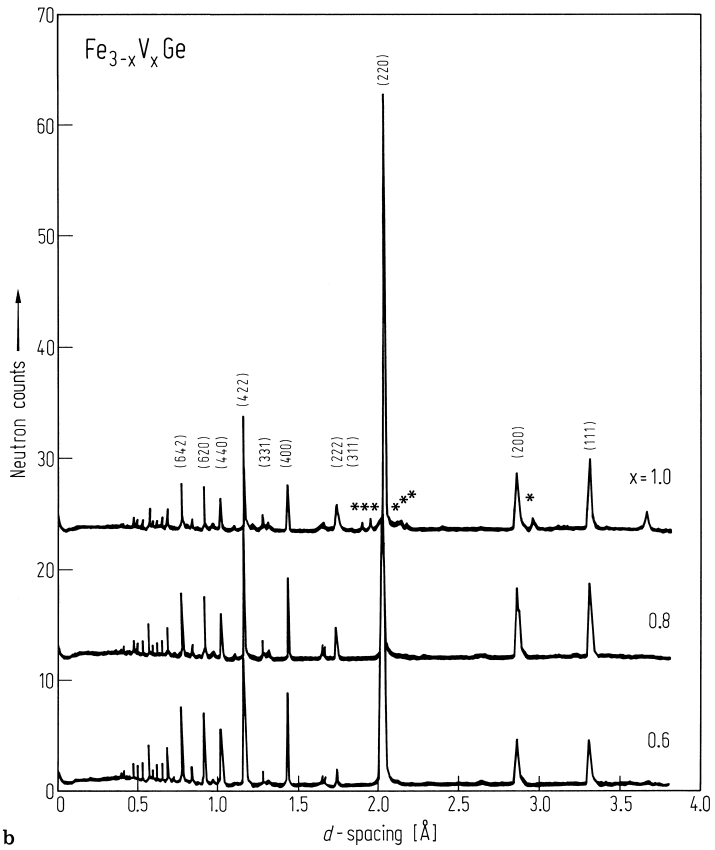

b

Fig. 201b.

Fe_2MnSi

Below 214 K the compound becomes ferromagnetic, but at 80 K the spontaneous magnetisation decreases, suggesting a canted structure [88W1]. The canted structure has (AF2) symmetry, but the absence of the (½½½) magnetic reflection suggests that the spin direction is parallel to the (111) direction.

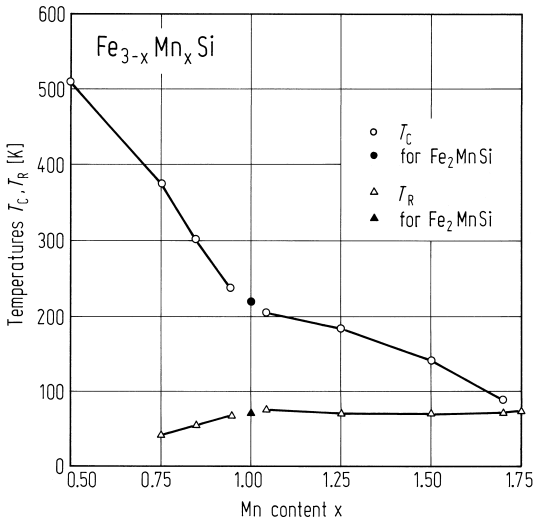

Fig. 202. The magnetic phase diagram of the $Fe_{3-x}Mn_xSi$ alloy system ($0 \leq x \leq 2$) showing the variation of the Curie temperature T_C and the magnetic re-ordering temperature (T_R) with Mn composition [95E1].

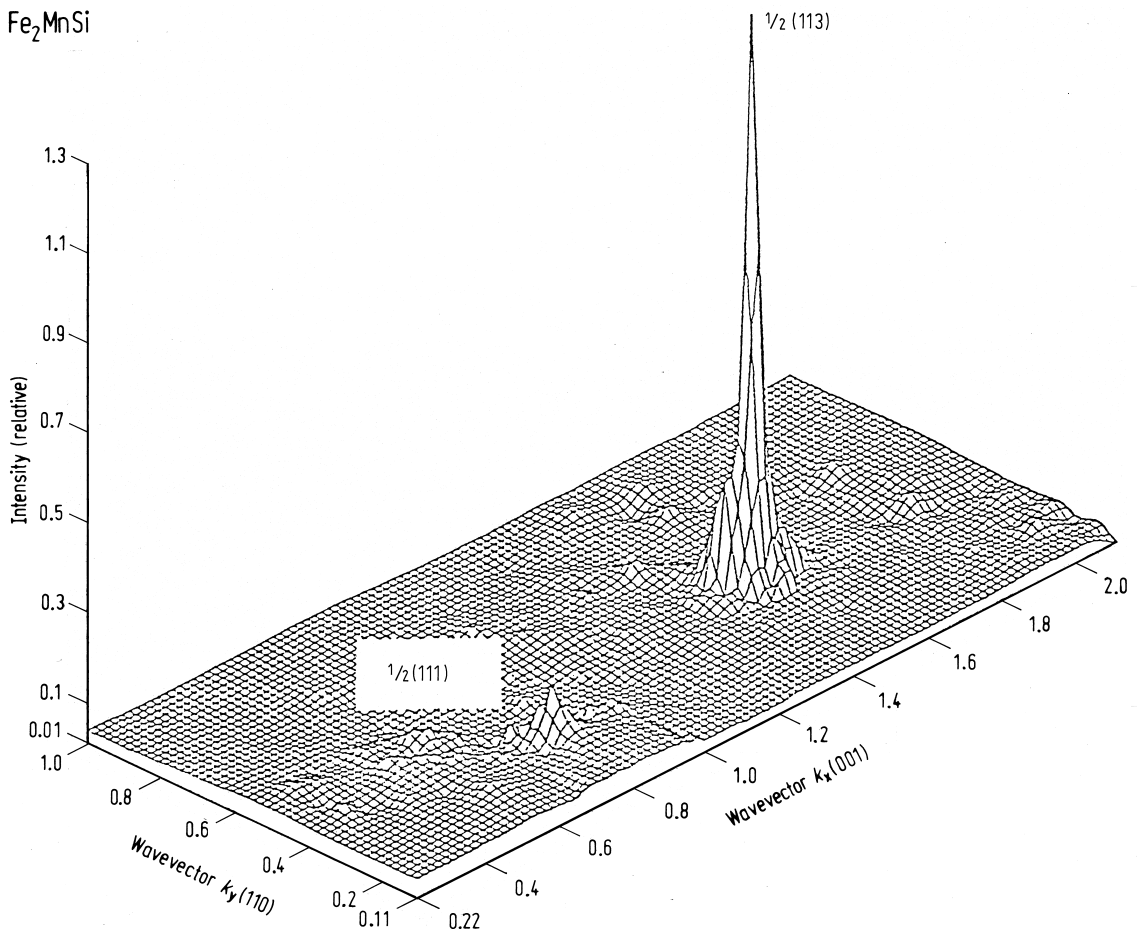

Fig. 203. Centered structure has been investigated using polarised neutrons. The spin flip scattering associated with the first two antiferromagnetic reflections is shown [95E1].

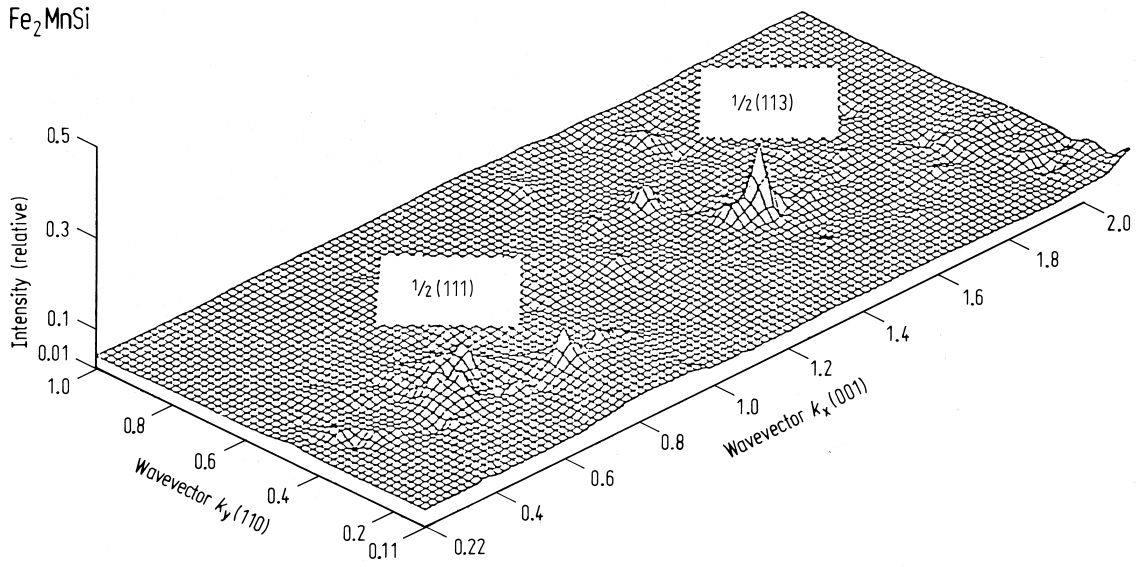

Fig. 204. Non-spin flip scattering profile of the ½ (113) antiferromagnetic Bragg peak [95E1].

X_2YZ X = 3d, Y = 3d

X = 7A: Mn; 8A: Ni
Y = 7A: Mn; 8A: Ni
Z = 4B: Sn

Ni_2MnSn - Mn_2NiSn

Ni_2MnSn is ferromagnetic below 360 K with a moment of 4.2 μ_B confined to the manganese atoms [88W1]. However, on forming Mn_2NiSn, the manganese atoms occupying tetrahedral sites have smaller moments aligned anti-parallel to the manganese moments on the octahedral sites [87H1].

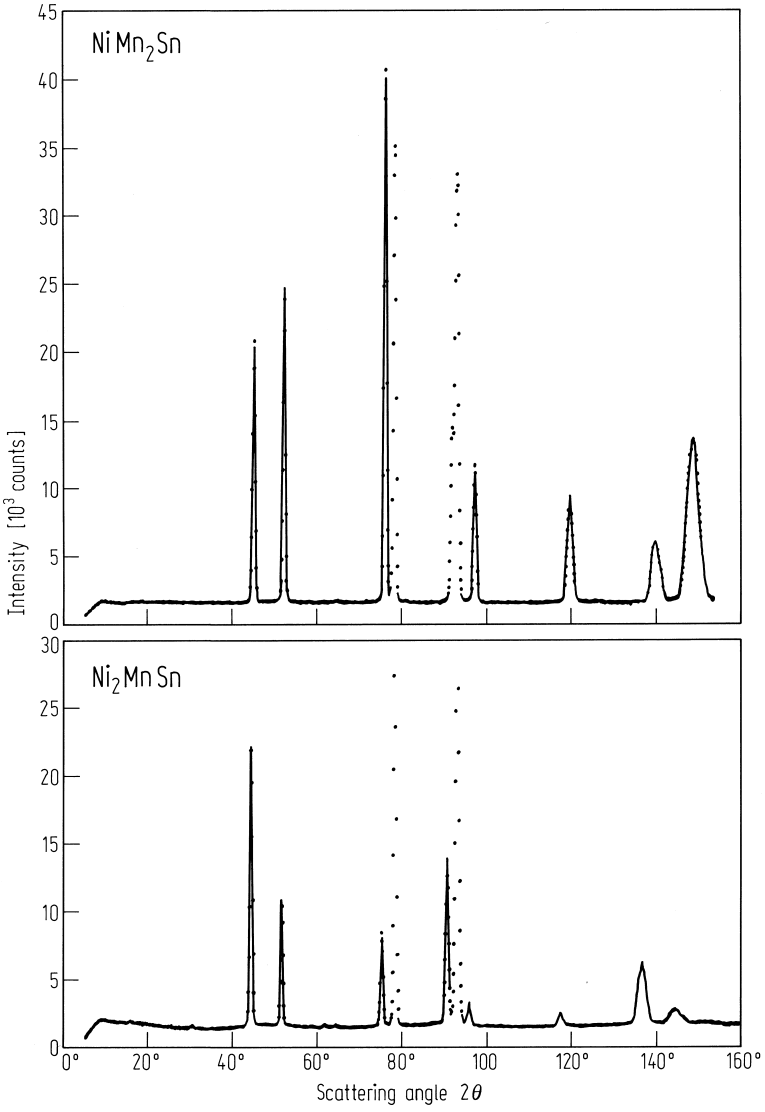

Fig. 205. Neutron diffraction patterns of $NiMn_2Sn$ (upper curve) and Ni_2MnSn (lower diagram) at 4.2 K. The full line represents a least squares fit to the data. Ni_2MnSn orders ferromagnetically with 5.04 μ_B located on the Mn atoms. The bulk moment of $NiMn_2Sn$ is 2.01 μ_B but the neutron results indicate a moment of 4.49 μ_B on those manganese atoms on their correct (octahedral) sites and a moment of –2.01 μ_B on the Mn atoms occupying tetrahedral sites. A summary of the diffraction results is given in Table 42 [87H1].

Table 42. Parameters associated with the refinement of the neutron diffraction patterns of Ni_2MnSn and $NiMn_2Sn$ at 4.2 K. Occupancy number n of the various sites, magnetic moment of the manganese atoms at the octahedral site (p_{oct}) and tetrahedral site (p_{tet}), total moment (p_{tot}), lattice constant a, temperature factor B, reliability factors R_{nucl} and R_{mag}. The quantity χ^2 is the chi square test [87H1].

Parameters	Ni_2MnSn	$NiMn_2Sn$
Ni n (0, 0, 0)	1.0	0.628(9)
Ni n (½, ½, ½)	1.0	0.372(9)
Ni n (¼, ¼, ¼)	0	0
Mn n (0, 0, 0)	0	0.372(9)
Mn n (½, ½, ½)	0	0.628(9)
Mn n (¼, ¼, ¼)	1.0	1.0
Sn n (¾, ¾, ¾)	1.0	1.0
p_{tot} [μ_B/f.u.]	5.04(10)	2.48
p_{oct} [μ_B/Mn atom]	5.04(10)	4.49(4)
p_{tet} [μ_B/Mn atom]	0	– 2.01(4)
a [nm]	0.60326(1)	0.60991(2)
B [10^2 nm]	– 0.42(5)	0.47(7)
R_{nucl} [%]	3.1	3.6
R_{mag} [%]	3.3	2.5
χ^2	13.6	8.7

X_2YZ X = 4d, Y = 3d

X = 8A: Ru, Pd; 1B: Ag
Y = 4A: Ti; 7A: Mn
Z = 3B: In; 4B: Ge; 5B: Sb

Pd_2TiIn

Around ≈ 110 K the compound has a broad anomaly in the specific heat. Although the effective Bohr magneton number above 110 K is 4.9 μ_B, neutron diffraction has failed to reveal any long-range magnetic order in the ground state [94O1].

Table 43. Atomic positions in the two crystallographic space groups for the face centred cubic $Fm\bar{3}m$ and the body centred tetragonal I4/mmm structures [94O1].

Face-centred cubic ($Fm\bar{3}m$)				Body centred tetragonal (I4/mmm)			
Atom	Site	Site symmetry	Atomic positions	Atom	Site	Site symmetry	Atomic positions
Ti	4a	$m\bar{3}m$	(0, 0, 0)	Ti	2a	4/mmm	(0, 0, 0)
In	4b	$m\bar{3}m$	(½, ½, ½)	In	2b	4/mmm	(0, 0, ½)
Pd	8c	$\bar{4}3m$	(¼, ¼, ¼)	Pd	4d	$\bar{4}m2$	(½, 0, ¼)
			(¼, ¼, ¾)				(0, ½, ¼)

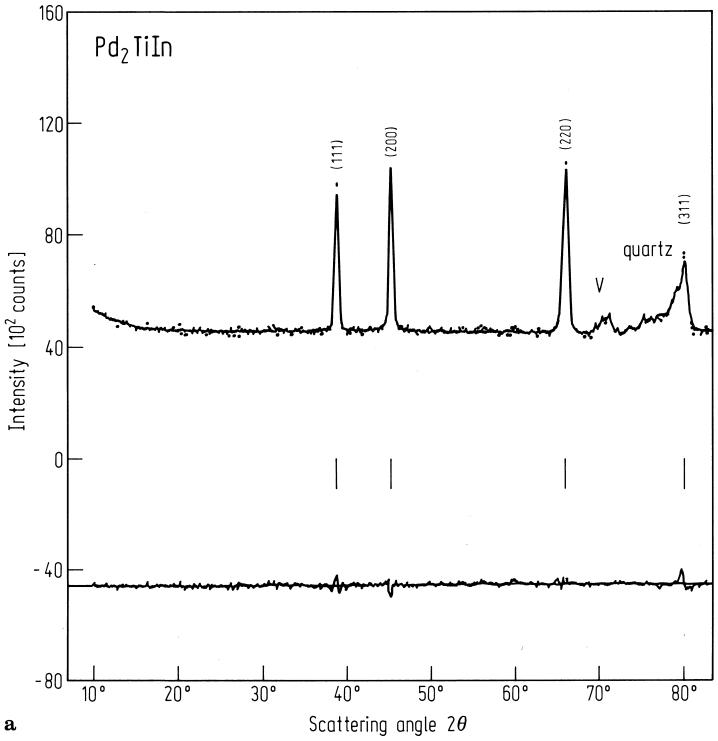

a

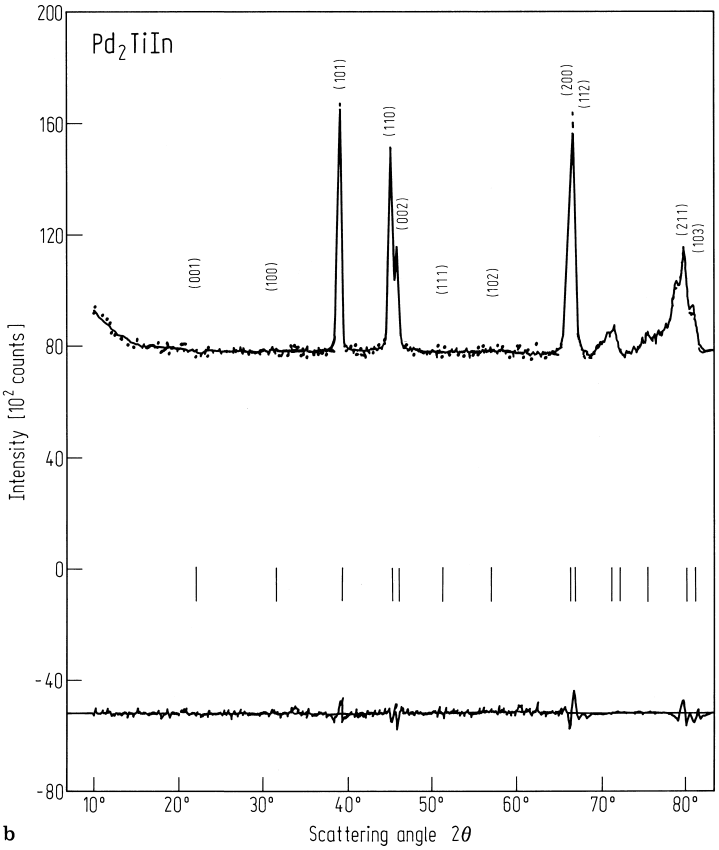

b

Fig. 206. Upper dotted and solid lines represent the observed and calculated diffraction patterns for Pd_2TiIn at (**a**) 300 K and (**b**) 4 K. Below the diffraction pattern the positions of the Bragg peaks are indicated by short vertical lines and the lowest curve represents the difference between the observed and calculated profiles [94O1].

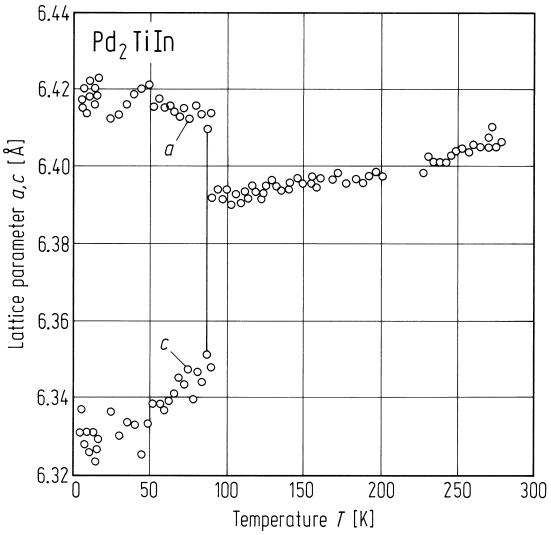

Fig. 207. Thermal variation of the lattice parameters of Pd_2TiIn showing a discontinuity at 92 K [94O1].

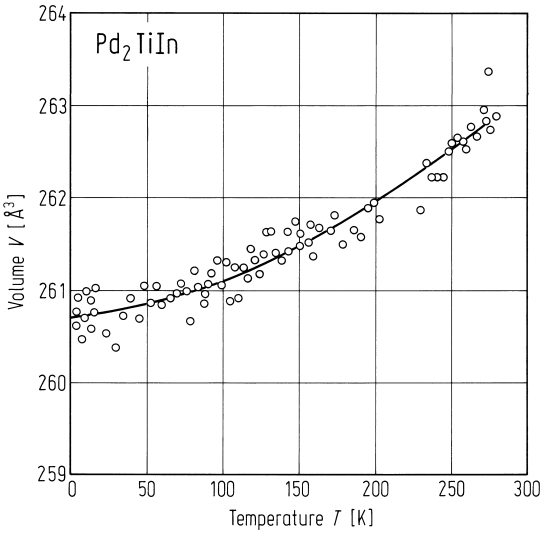

Fig. 208. Variation of unit cell volume as a function of temperature. It may be noted that there is no apparent change in volume at 92 K [94O1].

Ru_2MnSb and Ru_2MnGe

The magnetic structures of Heusler alloys based on manganese, and where X is a group 4d element, have predominantly concerned compounds containing palladium [88W1]. Ru_2MnSb and Ru_2MnGe have Néel temperatures of 200 K and 295 K, respectively [95G1].

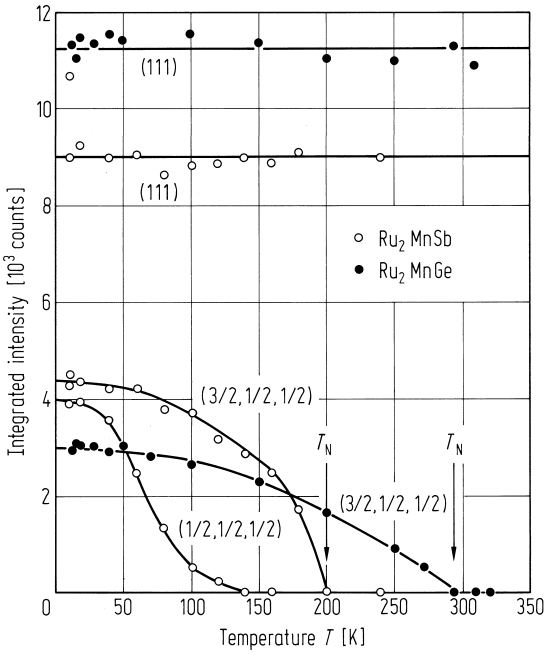

Fig. 210. Temperature dependence of the integrated intensities of the nuclear (111) reflection and the magnetic (½, ½, ½) ($^3/_2$, ½, ½) reflections for Ru_2MnSb and Ru_2MnGe [95G1].

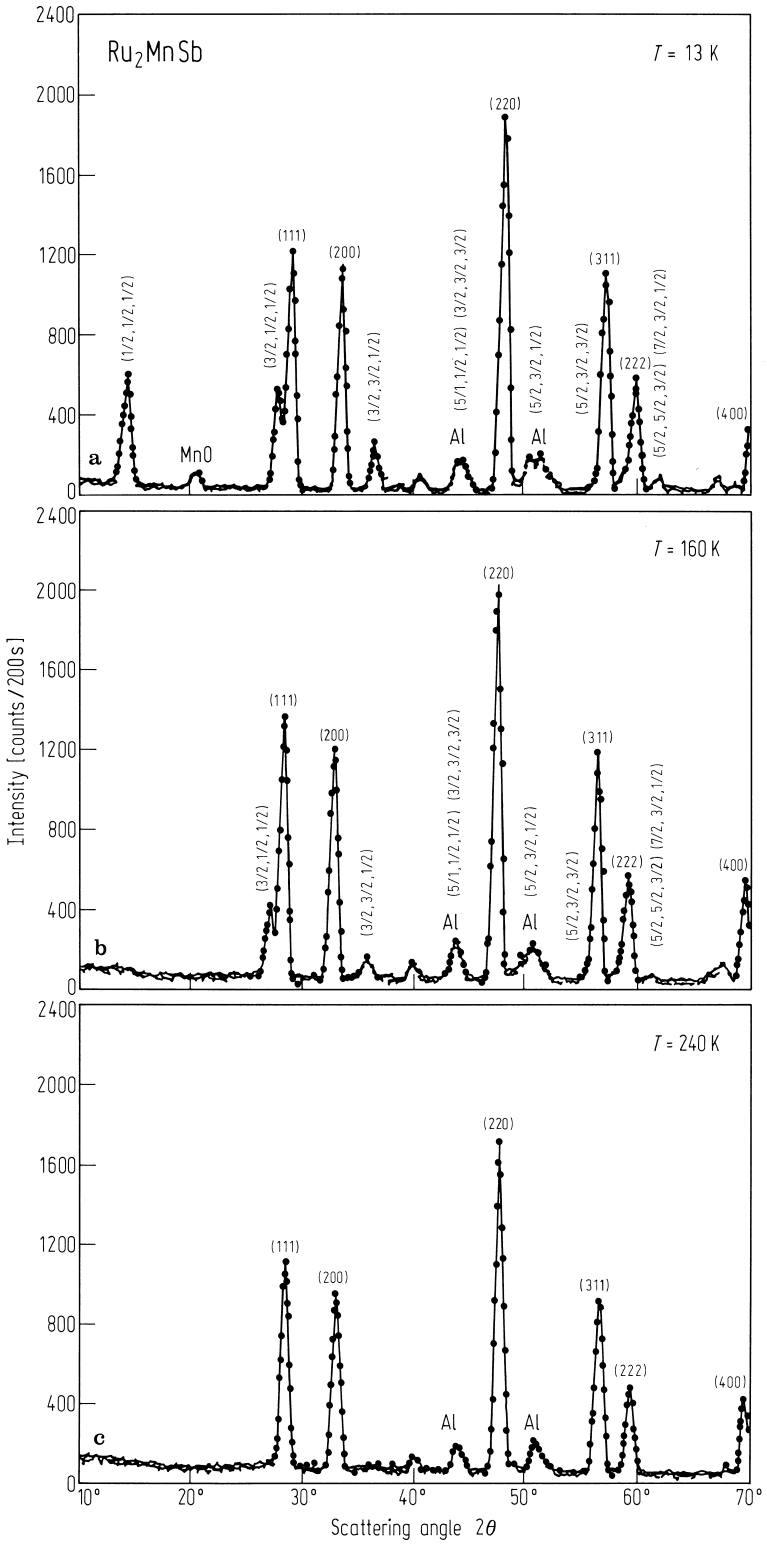

Fig. 209. Neutron diffraction pattern for Ru_2MnSb at 13 K (**a**), 160 K (**b**) and 240 K (**c**). A magnetic moment of 4.4 μ_B is confined to the Mn atoms. Above 100 K the moment direction is along (111) but deviates towards the (110) axis with decreasing temperature. The Néel temperature is 200 K. A similar AF2 structure was reported for Ru_2MnGe which has a Mn moment of 3.8μ_B and a Néel temperature of 295 K [95G1].

$Pd_{2-x}Ag_xMnIn$

Single phase alloys with the $L2_1$ form with $0 \leq x \leq 0.8$. As a function of increasing x, the system moves from the AF2 structure through AF3A to ferromagnetism at the Ag-rich end of the series. The substitution of Pd by Ag has a similar effect on the magnetic properties as the replacement of In by Sn in the $Pd_2MnIn_{1-x}Sn_x$ system [88W1].

Table 44. Magnetic structures and properties of $Pd_{2-x}Ag_xMnIn$ and related Heusler alloys [86W1].

Alloy	*a* [Å]	Magnetic structure	T_C or T_N [K]
Pd_2MnIn	6.373	AF2	142
$Pd_{1.6}Ag_{0.4}MnIn$	6.418	AF3A	≈ 150
$Pd_{1.2}Ag_{0.8}MnIn$	6.470	F	146
Pd_2MnSn	6.380	F	189
$Pd_2MnIn_{0.6}Sn_{0.4}$	6.381	AF3A	176
Pd_2MnSb	6.413	F	255
$Pd_2MnIn_{0.8}Sb_{0.2}$	6.381	AF3A	≈ 130
Cu_2MnIn	6.217	F	533
$Pd_{1.6}Cu_{0.4}MnIn$	6.352	AF3A	≈ 140

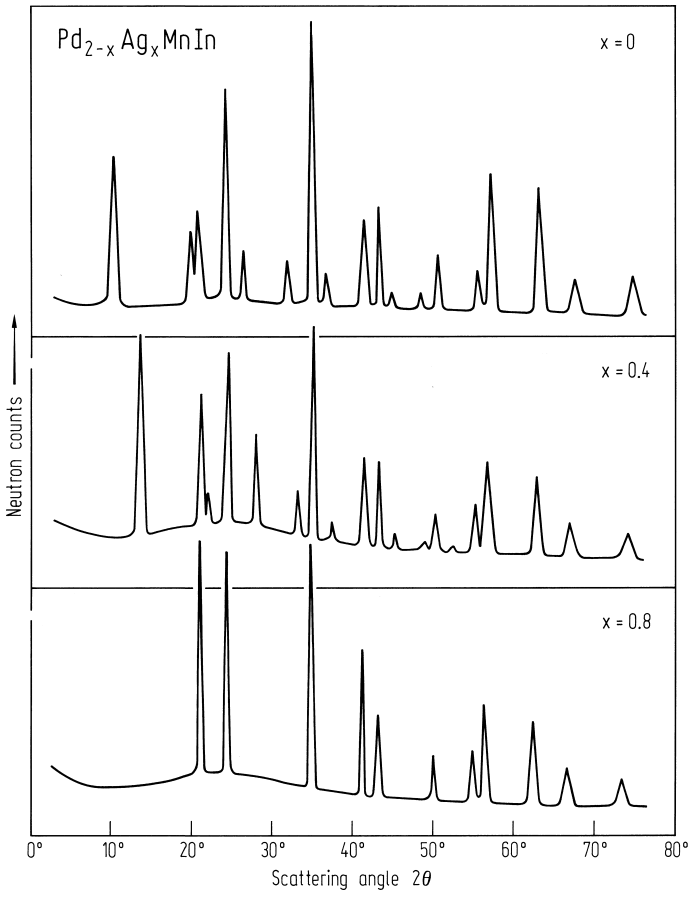

Fig. 211. Neutron diffraction patterns for intermetallic compounds in the series $Pd_{2-x}Ag_xMnIn$ at 4.2 K [86W1].

X_2YZ X = 4d, Y = 3d

X = 8A: Pd; 1B: Au
Y = 7A: Mn
Z = 3B: In

$Pd_{2-x}Au_xMnIn$

This series of compounds is the first reported in which antiferromagnetism type 1 (AF1) has been observed. In fact, depending upon composition, three types of antiferromagnetic structure occur.

Table 45. A summary of the magnetic properties and structures of $Pd_{2-x}Au_xMnIn$ alloys [92J1].

x	a [Å]	Θ [K]	T_C or T_N [K]	p_{eff} [μ_B]	Magnetic structure
0.0	6.373	50 ± 3	142 ± 3	4.30 ± 0.02	AF2
0.2	6.341	75 ± 3	142 ± 3	4.50 ± 0.02	AF2 + AF3A
0.4	6.349	85 ± 2	145 ± 3	4.60 ± 0.02	AF2 + AF3A
0.6	6.413	98 ± 2	143 ± 3	4.52 ± 0.02	AF1 + AF3A
0.8	6.448	109 ± 3	148 ± 2	4.75 ± 0.03	AF1 + AF3A
1.0	6.463	117 ± 3	150 ± 3	4.67 ± 0.02	AF1 + AF3A
1.2	6.522	126 ± 3	152 ± 2	4.68 ± 0.03	AF1 + AF3A
1.4	6.544	131 ± 3	155 ± 2	4.78 ± 0.02	AF1 + AF3A + F
1.6	6.566	139 ± 3	158 ± 2	4.85 ± 0.02	F
1.8	6.599	146 ± 2	163 ± 2	4.99 ± 0.03	F
2.0	6.644	152 ± 2	168 ± 2	5.04 ± 0.03	F

X_2YZ X = 4d, Y = 3d

X = 8A: Pd; 1B: Ag
Y = 4A: Ce, Nd, Sm, Tb, Dy, Ho, Er
Z = 3B: In; 4B: Sn

The ground state magnetic structure of compounds in which the moment is carried by a rare earth element depends upon the crystalline electric field (CF). Consequently, the magnitude of the moment is usually reduced from the free ion value.

Pd_2YSn

Pd_2DySn, Pd_2HoSn and Pd_2ErSn all order antiferromagnetically with AF2 structure below 7 K, 5 K and 1 K, respectively [87D1, 88L1, 87S4]. However, in the case of Pd_2DySn and Pd_2ErSn, the magnetic structures appear more complicated than the proposed collinear models [95C1, 87S4]. At 1.2 K the magnetic moments in the antiferromagnetic state are (6.7 ± 0.5) μ_B for Pd_2DySn and (4.4 ± 0.1) μ_B for Pd_2HoSn, much smaller than the free ion values of 10 μ_B [87D1].

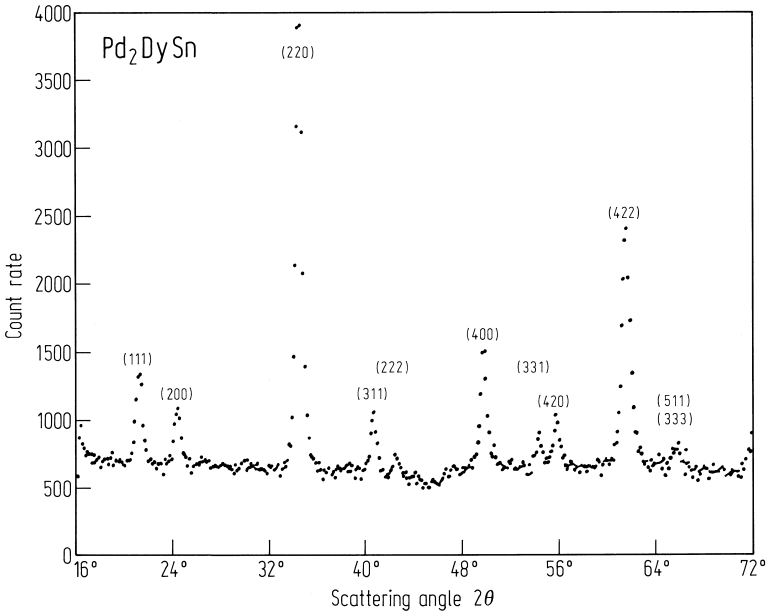

Fig. 212. Neutron diffraction patterns for Pd_2DySn at room temperature indicating the Heusler $L2_1$ structure in Pd_2DySn [87D1].

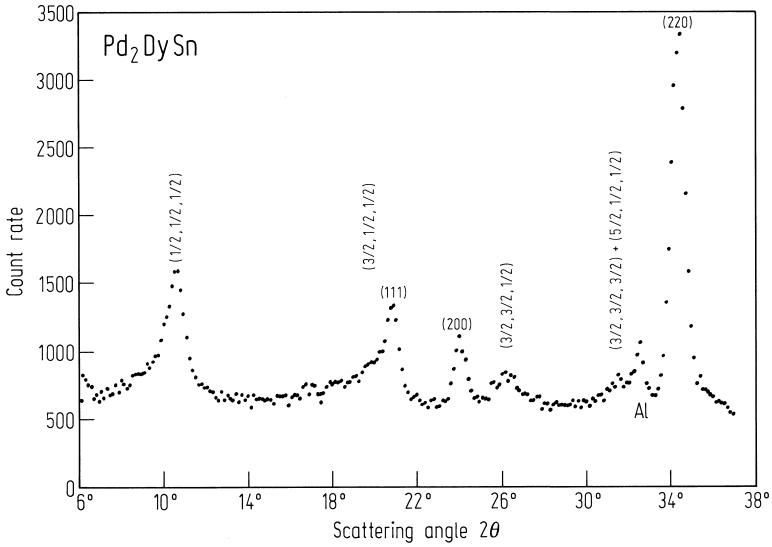

Fig. 213. Neutron diffraction pattern of Pd_2DySn at 4.2 K. The reflections with half indices are from the AF2 magnetic structure [87D1].

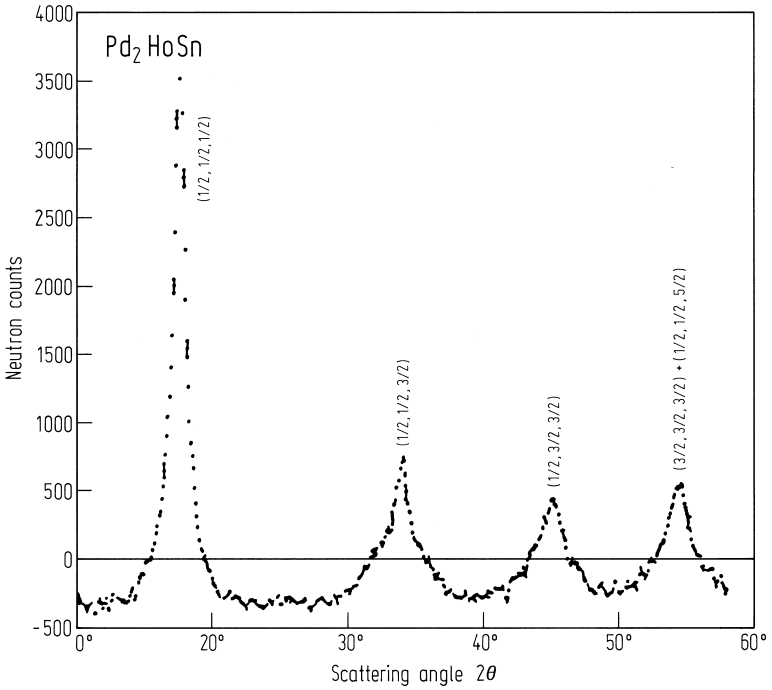

Fig. 214. Magnetic powder diffraction pattern for Pd_2HoSn obtained by subtracting the data measured at T = 6 K from the data at T = 0.44 K. The Néel temperature is 5 K and the magnetic structure is AF2 [88L2].

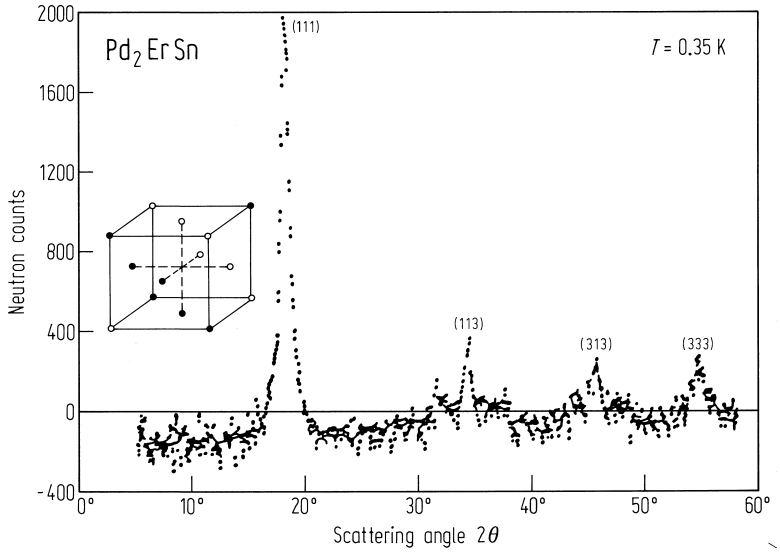

Fig. 216. Magnetic powder diffraction pattern for Pd_2ErSn. The AF2 structure for an fcc lattice is shown in the inset. Filled and open circles correspond to two possible (collinear) spin directions. Satellite reflections indicate that in fact the structure is modulated [87S4].

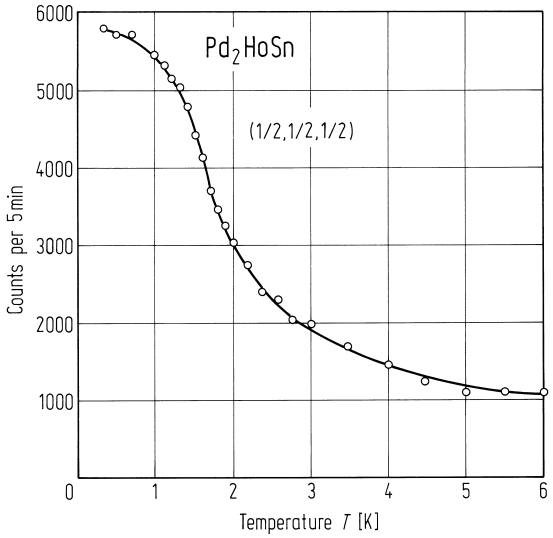

Fig. 215. Temperature dependence of the (½, ½, ½) antiferromagnetic peak intensity in Pd_2HoSn. The Néel temperature is 5K [88L2].

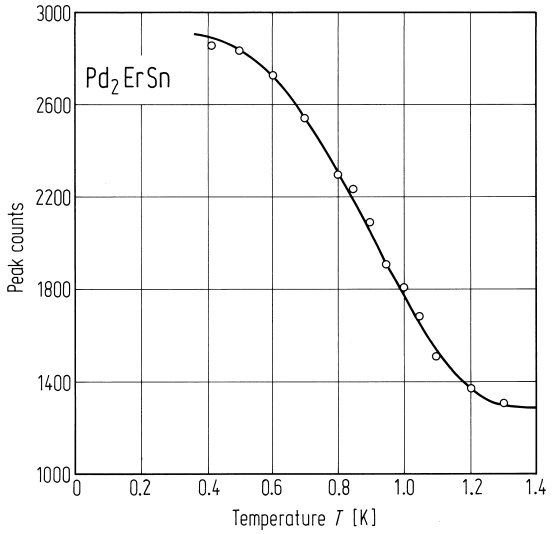

Fig. 218. Temperature dependence of the peak intensity of (111) magnetic reflection for Pd_2ErSn [87S4].

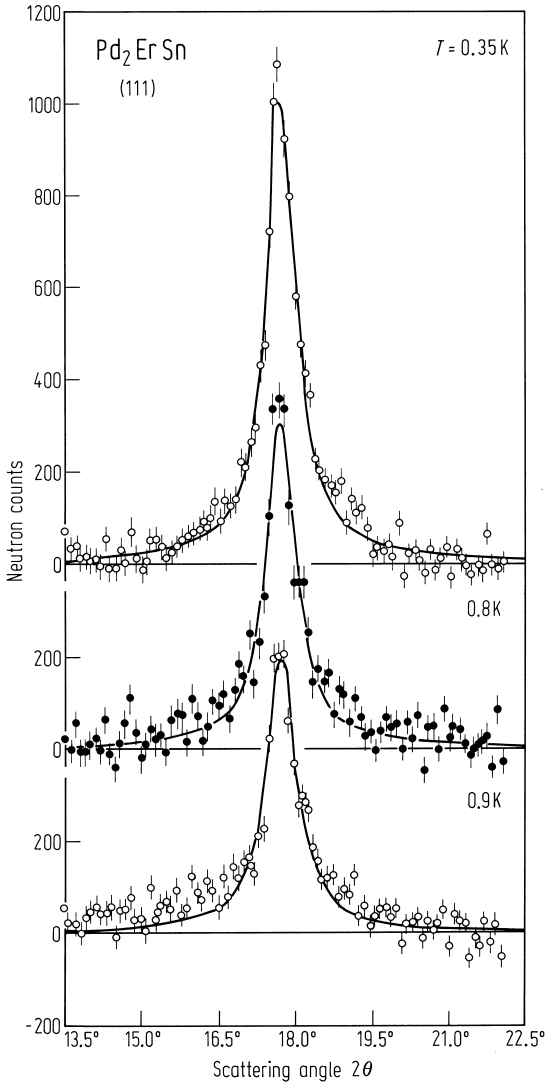

Fig. 217. Temperature dependence of the (111) magnetic peak indicating a Néel temperature of 1K. The compound Pd_2ErSn becomes superconducting at 1.17 K [87S4]. E_F = 14.8 meV.

Ag_2YIn

Compounds with R = Ce, Nd, Sm, Gd, Tb and Dy order antiferromagnetically at low temperatures. Neutron diffraction measurements indicate that Ag_2CeIn [82G1] orders antiferromagnetically with the commensurate fcc type 1 structure. Of the remaining compounds measurements down to 1.6 K failed to reveal any long-range magnetic order in Ag_2DyIn. Ag_2TbIn was found to have a temperature dependent incommensurate structure. Between 1.6 K and 6 K the magnetic structure is reported as being cycloidal and between 6 K and 8.3 K it has a sinusoidal arrangement [92A1].

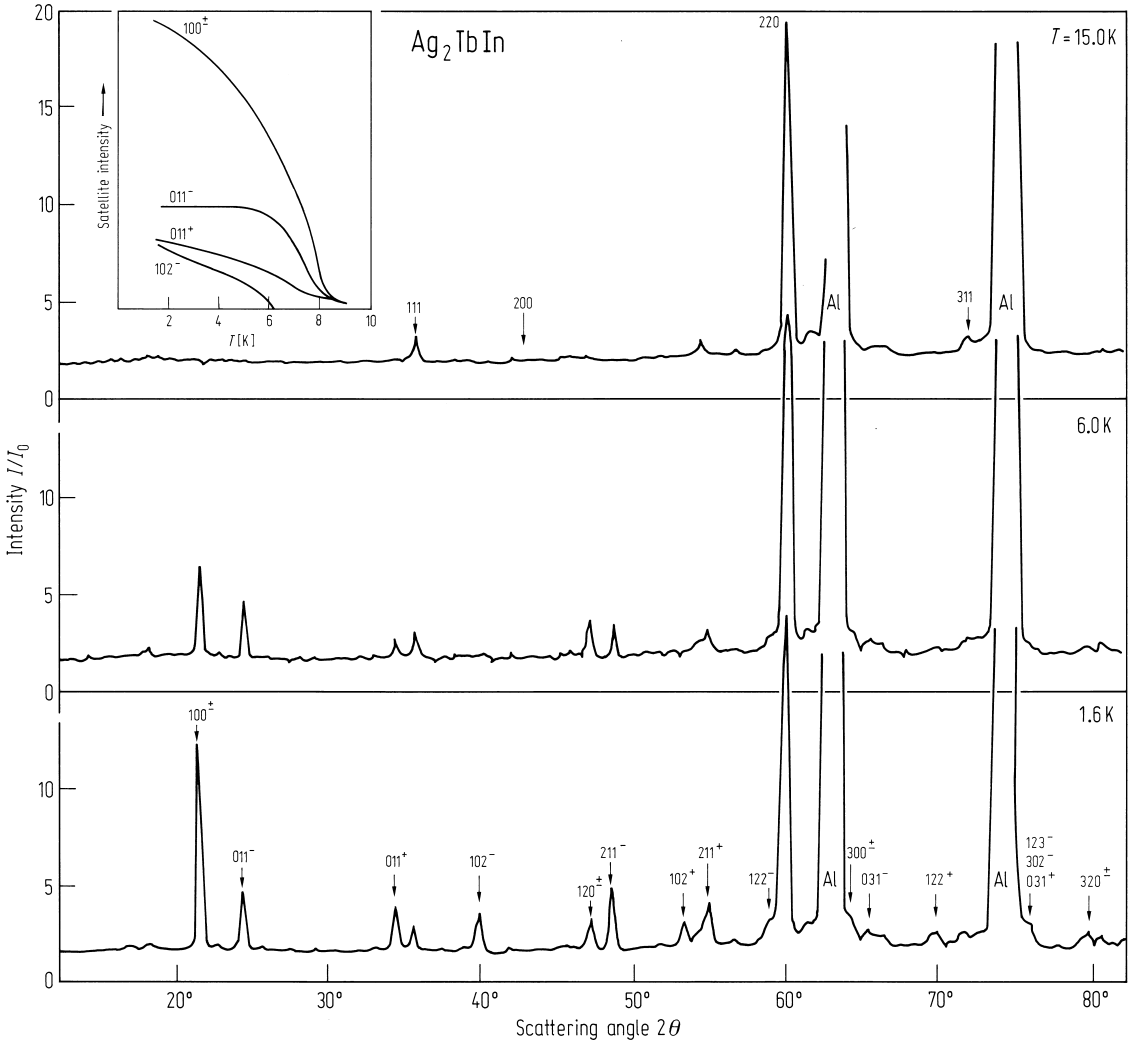

Fig. 219. Neutron diffraction patterns of Ag_2TbIn at 1.6, 6 and 15 K. The inset shows the temperature dependence of the $100^{\pm}$, 011^{-}, 011^{+}, and 102^{-} satellite intensities [92A1].

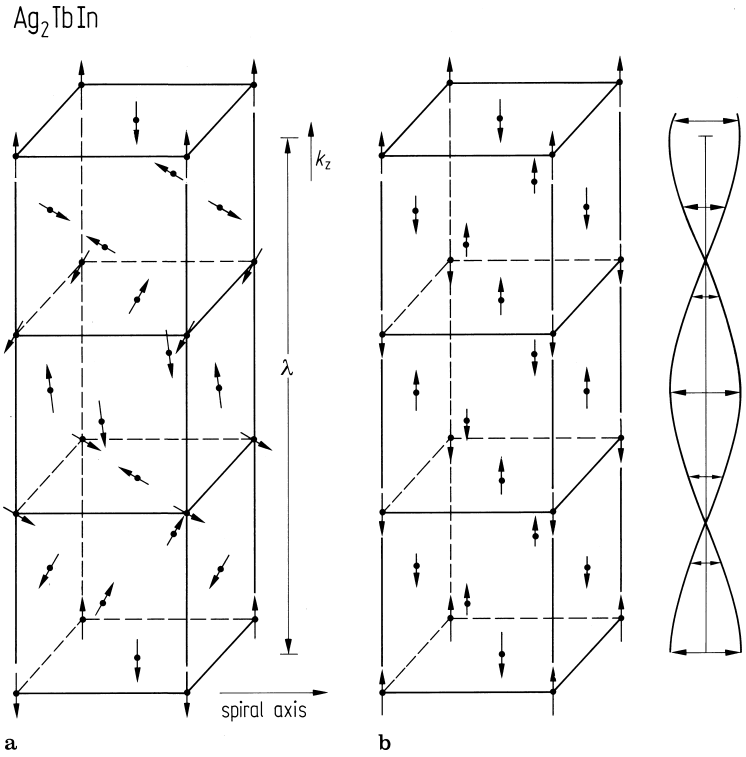

Fig. 220. Magnetic structure of Ag_2TbIn in (**a**) the cycloidal phase 1.6 to 6 K and (**b**) in the sinusoidal phase between 6 and 8.3 K. The magnetic moment per Tb atom at 1.6 K is observed to be 5.6 (2) μ_B much smaller than the free ion value of $g_J J = 9\ \mu_B$, suggesting a strong influence of CEF [92A1].

$C1_b$ XYZ

$C1_b$ compounds are formed at the stoichiometric composition XYZ with the tetrahedral sites being void. Compounds with this structure often have Z = Sb, although some $C1_b$ compounds form with Ga and Sn. The structure has space group F43m and therefore does not have a centre of inversion symmetry.

X = 8A: Ni, Ir
Y = 7A: Mn
Z = 3B: Ga; 5B: Sb

Table 46. Various possibilities of the site occupancy in NiMnSb and the comparison with the observed diffraction pattern (Fig. 221). The quality of agreement between the calculated and observed diffraction pattern on the basis of the site occupancy is given by the chi square test and the *R* factor [84H1].

No.	(0, 0, 0)	(¼, ¼, ¼)	(½, ½, ½)	(¾, ¾, ¾)	χ^2_γ	*R* factor
1	Ni	Mn	–	Sb	25	3.1
2	Ni		Mn	Sb	472	25
3	(Ni,Mn)	(Ni,Mn)	–	Sb	1201	65
4	Ni	–	(Mn,Sb)	(Mn,Sb)	519	43.7
5	(Ni)	(Ni)	Mn	Sb	457	41.4
6	(Ni)	(Ni)	(Mn,Sb)	(Mn,Sb)	988	56.4
7	Ni	(Mn,Sb)	–	(Mn,Sb)	95	17.2

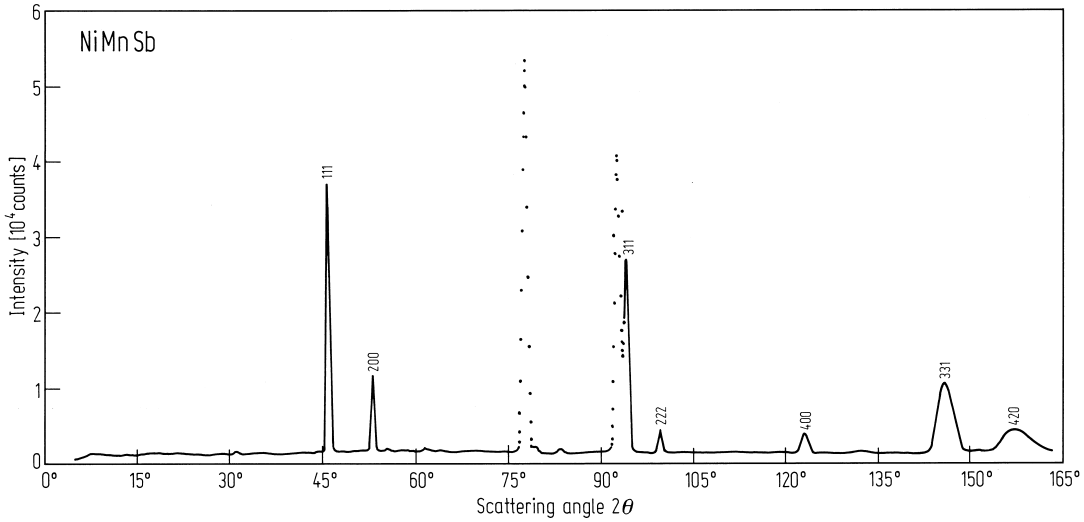

Fig. 221. Neutron diffraction pattern of NiMnSb at 4.2 K. The solid line represents a least square fit to the observation. The details of the model are given in Table 46 [84H1].

Table 47. A summary of the possible site occupancies in IrMnGa and a comparison of the model calculation with observation [84H1].

No.	(0, 0, 0)	(¼, ¼, ¼)	(½, ½, ½)	(¾, ¾, ¾)	χ^2_γ	*R* factor
1	Ir	Mn	–	Ga	52	42
2	Ir	–	Mn	Ga	66	51
3	Ga	(IrMn	–	IrMn)	7.2	14.0
4	Ga	(IrMn	–	IrMn)	6.2	10.3
5	(IrMn)	(IrMn)	–	Ga	57	48
6	(IrMn)	(IrMn)	–	Ga	2.1	3.7

Table 48. Results of the refinement of the magnetic neutron diffraction data at 4.2K [84H1]. *R*: reliability factor.

Compound	R_{mag}	p_{Mn} [μ_B]	*a* [Å]
NiMnSb	2.3	4.0	5.913
IrMnGa	3.9	0.6	6.023

Table 49. Various possibilities of site occupancy in NiMnSb. The ΔE values represent total energies calculated with respect to the most stable structure (No. 1) in kcal mol^{-1}. The theoretically derived values of the magnetic moments are listed under *M* in μ_B [84H1].

No.	(0, 0, 0)	(¼, ¼, ¼)	(½, ½, ½)	(¾, ¾, ¾)	ΔE	*M*
1	Ni	Mn	–	Sb	0	4.00
2	Mn	Ni	–	Sb	420	3.32
3	Ni	–	Mn	Sb	503	3.11